

Non-thermal Sunyaev-Zeldovich signal from radio galaxy lobes

Sandeep Kumar Acharya,¹★ Subhabrata Majumdar,¹† Biman B. Nath²‡

¹*Department of Theoretical Physics, Tata Institute of Fundamental Research, Mumbai 400005, India*

²*Raman Research Institute, Sadashiva Nagar, Bangalore 560080, India*

Accepted XXX. Received YYY; in original form ZZZ

ABSTRACT

Energetic electrons in the lobes of radio galaxies make them potential sources for not only radio and X-rays but also Sunyaev-Zeldovich (SZ) distortions in the cosmic microwave background (CMB) radiation. Previous works have discussed the energetics of radio galaxy lobes, but assuming thermal SZ effect, coming from the non-thermal electron population. We use an improved evolutionary model for radio galaxy lobes to estimate the observed parameters such as the radio luminosity and intensity of SZ-distortions at the redshifts of observation. We, further, quantify the effects of various relevant physical parameters of the radio galaxies, such as the jet power, the time scale over which the jet is active, the evolutionary time scale for the lobe, etc on the observed parameters. For current SZ observations towards galaxy clusters, we find that the non-thermal SZ distortions from radio lobes embedded in galaxy clusters can be non-negligible compared to the amount of thermal SZ distortion from the intra-cluster medium and, hence, can not be neglected. We show that small and young (and preferably residing in a cluster environment) radio galaxies offer better prospects for the detection of the non-thermal SZ signal from these sources. We further discuss the limits on different physical parameters for some sources for which SZ effect has been either detected or upper limits are available. The evolutionary models enable us to obtain limits, previously unavailable, on the low energy cut-off of electron spectrum ($p_{min} \sim 1-2$) in order to explain the recent non-thermal SZ detection. Finally, we discuss how future CMB experiments, which would cover higher frequency bands (>400 GHz), may provide clear signatures for non-thermal SZ effect.

Key words: Cosmology: cosmic background radiation - galaxies: jets - galaxies: evolution

1 INTRODUCTION

Studying the distortion of the cosmic microwave background radiation (CMB) through the Sunyaev-Zel'dovich effect (SZ effect) (Zeldovich & Sunyaev 1969) has become a mainstay of modern cosmology. The inverse Compton scattering of the CMB photons by energetic electrons has opened up a new window of probing the warm and hot gaseous regions of the universe (Birkinshaw 1999; Aghanim et al. 2008; Mroczkowski et al. 2019). Being complementary to the traditional X-ray observation of these ionized regions, SZ effect not only enables a robust determination of their physical properties, but also makes it possible to study them at high redshift, and consequently, study their evolution. The intensity of distortion of CMB does not dilute with increasing redshift resulting from the fact that the energy density of scattered CMB photons and the intensity of CMB photons have same functional dependence on redshift.

Besides energetic thermal electrons in hot gas, non-thermal relativistic gas can also produce SZ signal, whose distinct spectral signature makes it an interesting probe of reservoirs of such gas in the universe (EnBlin & Kaiser 2000; Majumdar 2001). One source of energetic particles can be radio galaxy lobes where relativistic particles are supplied by the radio jet (Scheuer 1974; Begelman & Cioffi 1989; Nath 1995), which was first predicted by Felten & Rees (1969)

soon after the discovery of CMB. The pressure from the energetic particles can push out the surrounding gas with the size of the radio lobe growing to megaparsec length scales (Baldwin 1982; Kaiser et al. 1997). Recent detection of X-ray emission from radio lobes has been explained through inverse Compton scattering of CMB photons by non-thermal relativistic electrons that are responsible for the radio emission (Croston et al. 2005; Erlund et al. 2008; Fabian et al. 2009; Johnson et al. 2007; Isobe et al. 2009). These studies have utilized the fact that relativistic non-thermal electrons are the source for both the X-ray and the radio emission, and can therefore deduce the magnetic fields in these objects with greater confidence than were previously possible (Isobe et al. 2009). At the same time, the inverse Compton X-ray points towards a concomitant distortion in the CMB.

The non-thermal SZ effect from radio galaxies was studied by Colafrancesco (2008) by inferring the shape of electron spectrum from the observed X-ray signal. This idea was further extended by Colafrancesco & Marchegiani (2011) by using X-ray and radio signal from radio galaxies. The authors concluded that non-thermal SZ signal gives a reliable understanding of the low energy cutoff of the electron spectrum to which X-ray and radio signals are insensitive. Following this idea, there have been searches for non-thermal SZ signal towards radio galaxies, which have fetched upper limits (Colafrancesco et al. 2013) until a recent detection (Malu et al. 2017). The shape of this distortion is a function of non-thermal spectrum of these relativistic particles (Birkinshaw 1999; EnBlin & Kaiser 2000) and is distinct from the shape of the thermal γ -distortion (Zeldovich & Sunyaev 1969). In previous works, Yamada et al. (1999) & Ma-

★ sandeepkumar@theory.tifr.res.in

† subha@tifr.res.in

‡ biman@rri.res.in

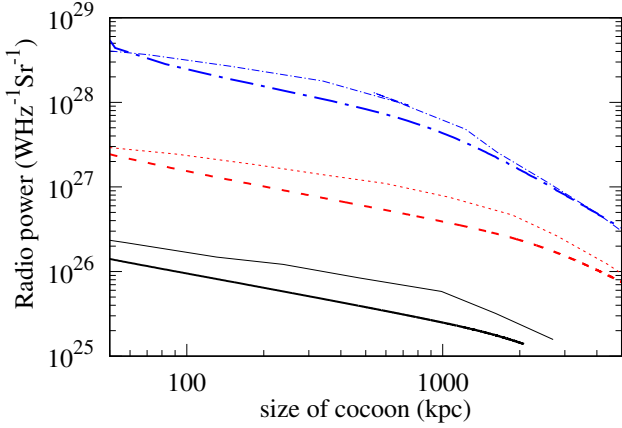


Figure 1. Comparison of radio power, at 150 MHz, obtained in this work (in thick lines) with the corresponding values in KDA1997 (thin lines) for the three cases as given in KDA1997 (their Fig. 1). The parameters for the blue (dot-dashed), red (dashed) and black (solid) lines correspond to $[Q_J$ (erg s $^{-1}$), z] = $[(10^{47}, 2), (10^{46}, 0.5) \& (10^{45}, 0.2)]$ respectively where Q_J is the jet luminosity and z is the observed redshift of radio galaxy. The spectral index of electron energy is taken to be $\alpha_p = 2.15$.

jumdar (2001) had estimated the global γ -distortion caused by radio galaxies to be $\approx 10^{-5}$, using a simple model of radio galaxy evolution and cosmological population of radio galaxies constructed from the Press-Schechter mass function.

In this paper, we first present an improved model for the evolution of radio galaxies in order to predict the non-thermal SZ signal from radio galaxy lobes which can be targets for upcoming SZ observations. We use the galaxy evolution model of *Kaiser et al. (1997)* (KDA1997 hereafter) with suitable modification for jet stopping as in *Nath (2010)* (N2010 hereafter). We explicitly keep track of the evolution of the relativistic particles. We then calculate the non-thermal SZ spectrum from these population of relativistic particles. Using the procedure detailed in this work, future observations of non-thermal SZ effect can be used to put constraints on the underlying physical model of radio galaxies, for example, that on the jet luminosity and lifetime, as also on the nature of relativistic population of electrons driven out by the radio jet, for example, the lowest energy threshold of the electron spectrum. The rest of the paper is arranged as follows. In Sec 2 we lay down our model for the radio galaxy lobes, followed by physics related to SZ distortions from non-thermal relativistic population of electrons in Sec 3. These are combined to estimate the non-thermal SZ from radio galaxy lobes in Sec 4. Next, Sec 5 & 6 discuss the degeneracies in model parameters and the prospects of future detection of non-thermal SZ effect. We discuss our results in 7 and, finally, conclude in 8. For calculating the angular diameter distance in converting angular to physical size we use $H_0 = 67$ km s $^{-1}$ Mpc $^{-1}$, $\Omega_M = 0.32$, $\Omega_\Lambda = 0.68$ (*Aghanim et al. 2018*).

2 MODEL FOR RADIO GALAXY LOBES

We start by assuming that the jet of the radio galaxy, which has a luminosity Q_J , injects relativistic particles throughout the jet lifetime t_J ($\approx 10^{7-8}$ yr), after which it ceases to be active. The injected energy causes a lobe around the jet to expand against the surrounding medium. We describe the density profile of the surrounding gas with a power law, $\rho(r) = \rho_0 (\frac{r}{r_0})^{-\beta_g}$ with $\beta_g = 2$ (*Wang & Kaiser 2008*). This density profile can be written as, $\rho(r) = \Lambda r^{-2}$, with $\Lambda = 10^{19} g$

cm $^{-1}$ (*Fukazawa et al. 2004; Jetha et al. 2007*). The non-thermal electron energy distribution in the radio lobe is assumed to be a power law with, $n(\gamma_i, t_i) = n_0 \gamma_i^{-\alpha_p} d\gamma_i$, where γ_i is the Lorentz factor of electrons at time of injection t_i , and α_p is the spectral index. We assume the minimum $\gamma_{\min} = 1$ and the maximum, $\gamma_{\max} = 10^6$. The evolution of the radio galaxy lobes can be described by (*Reynolds & Begelman 1997*),

$$Q_J(t) = \frac{1}{\Gamma_c - 1} (V_c \dot{p}_c + \Gamma_c p_c \dot{V}_c), \quad \frac{dL_J}{dt} = \left(\frac{p_c}{\rho} \right)^{1/2}, \quad (1)$$

where $Q_J(t)$ is the jet luminosity which is non-zero when jet is on ($t < t_J$, where t_J is the jet lifetime) and zero for $t > t_J$, $\Gamma_c = \frac{4}{3}$, V_c is the volume of the radio lobe, p_c is the pressure in the radio lobe, L_J is the fiducial size of the lobe and ρ is the density of surrounding gas. We assume the axial ratio of the cylinder shaped radio lobe to be $R = 2$, the average observed ratio (*Leahy & Williams 1984*). The volume of the lobe is then given by,

$$V_c = \frac{\pi}{4R^2} L_J^3. \quad (2)$$

The magnetic and particle energy densities in the lobe are given by,

$$U_B(t) = \frac{A p_c(t)}{(\Gamma_c - 1)(1 + A)}, \quad U_e(t) = \frac{p_c(t)}{(\Gamma_c - 1)(1 + A)}, \quad (3)$$

where $A = (1 + \alpha_p)/4$ (*Kaiser & Alexander 1997*). For a comparison with result of KDA1997, we first consider the case when jet is on all the time. We then proceed to compute the radio flux density at 150 MHz as a function of time or size of the radio lobe. Assuming that for synchrotron radiation, an electron emits only at the frequency $\nu = \gamma^2 \nu_L$, where ν_L is the Larmor frequency, we calculate the number density of electrons with Lorentz factor $\gamma_{150\text{MHz}}$ which will emit at 150 MHz as a function of time t . We then find the value of γ_i which were injected at time $t_i < t$ and which would have cooled to $\gamma_{150\text{MHz}}$ at time t . The equation for evolution of electron Lorentz factor γ is given by,

$$\frac{d\gamma}{dt} = -\frac{1}{3} \frac{1}{V_c} \frac{dV_c}{dt} - \frac{4}{3} \frac{\sigma_T}{m_e c} \gamma^2 (U_B + U_C), \quad (4)$$

where σ_T is Thomson cross-section, m_e is the mass of electron, c is the speed of light, U_B , U_C are the magnetic energy density and CMB energy density, respectively. This equation assumes no re-acceleration of electrons (since the RHS is negative). The normalization of particle spectrum n_0 at time t_i is given by (*Kaiser et al. 1997; Nath 2010*),

$$n_0(t_i) = \frac{U_e(t_i)}{m_e c^2} \int_{\gamma_{\min}}^{\gamma_{\max}} (\gamma_i - 1) \gamma_i^{-\alpha_p} d\gamma_i. \quad (5)$$

The number density of electrons with $\gamma = \gamma_{150\text{MHz}}$, at time t due to the expansion of radio lobe, is given by,

$$n(\gamma) = n_0 \frac{\gamma_i^{2-\alpha_p}}{\gamma^2} \left(\frac{p_c(t_i)}{p_c(t)} \right)^{-1}, \quad (6)$$

where $\frac{1}{V_c} \frac{dV_c}{dt} = \frac{3}{L_J} \frac{dL_J}{dt}$ and the radio lobes are assumed to evolve self-similarly (as warranted by the assumption of a constant axial ratio). Any volume segment of the radio lobe at time t can be related to pressure at time t_i as,

$$\delta V(t) = \frac{(\Gamma_c - 1) Q_J}{p_c(t_i)} (4R^2)^{(1-\Gamma_c)/\Gamma_c} \left(\frac{p_c(t)}{p_c(t_i)} \right)^{1/\Gamma_c} \delta t_i, \quad (7)$$

where δt_i is the time interval over which electrons were injected. Then, the power emitted at t at 150 MHz is given by,

$$P_\nu = \int_0^t \frac{1}{6\pi} \sigma_T c U_B \frac{\gamma_{150\text{MHz}}^3}{\nu} n(\gamma_{150\text{MHz}}) \delta V, \quad (8)$$

x	$p_{\min} = 1$	3	5	10
0.47 (27 GHz)	-0.16	-0.028	-0.011	-0.003
0.7 (39 GHz)	-0.33	-0.055	-0.021	-0.005
1.7 (93 GHz)	-1.08	-0.18	-0.068	-0.018
2.54 (145 GHz)	-1.3	-0.22	-0.086	-0.023
4.1 (225 GHz)	-0.72	-0.17	-0.069	-0.019
5.0 (280 GHz)	-0.2	-0.1	-0.05	-0.013

Table 1. Value of $g_{\text{NT}}(x)$ as in Fig. 2 at the frequency band of Simons Observatory (Ade et al. 2019).

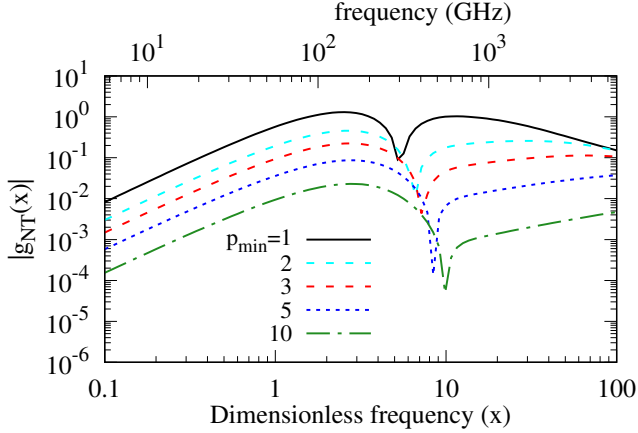


Figure 2. Absolute value of spectral function $g_{\text{NT}}(x)$ for power law distribution of electrons number density ($f_e(p) \propto p^{-\alpha_p}$) with $\alpha_p = 3$. The lowest momentum cutoff is denoted by p_{\min} and the highest momentum cutoff is chosen to be $p_{\max} \sim 10^6$. In magenta line, we show the $g_{\text{NT}}(x)$ for $\alpha_p = 2.3$ and $p_{\min} = 1$. The cuspy feature is due to changing sign of $g_{\text{NT}}(x)$ with $g_{\text{NT}}(x)$ being negative in value to the left of the cusp and positive to the right of the cusp. Note, $p = \sqrt{(\gamma^2 - 1)}$.

where the integral is done over electron injection time t_i . For jet shutdown at time t_j , the upper limit of integral should be $\min(t, t_j)$ (Nath 2010).

In Fig. 1, we have compared our results with the result of KDA1997 with the jet on for all the time for three different cases. The differences between the solid (this work) and dashed (KDA1997) lines are due to the fact that we have used equation 1 instead of using a power-law solution ($L_J \propto t^{3/5-\beta}$) at all times. A higher jet luminosity increases the radio power due to a larger number of energetic particles. This, also, increases the size of the lobe due to an increase in pressure owing to these particles. The initial expansion of the lobe is dominated by the pressure of the energetic particles and the synchrotron and inverse Compton cooling can be ignored. However, once the pressure drops due to expansion of the lobe, the inverse Compton cooling becomes important. At higher redshifts, cooling by CMB photons become increasingly efficient as CMB energy density is proportional to $(1+z)^4$. This can be seen in the leftward shift in the break of slope of the curve at ~ 1000 kpc since there are less number of energetic electrons at $\gamma_{150\text{MHz}}$ due to efficient cooling.

3 SUNYAEV-ZELDOVICH EFFECT FROM NON-THERMAL RELATIVISTIC POPULATION OF ELECTRONS

It is well known that energetic electrons can boost the CMB photons to higher energy through inverse Compton scattering creating a distortion in the CMB blackbody spectrum. If the energy distribution of

the electrons is non-relativistic and thermal, then the distortion has y-distortion shape (Zeldovich & Sunyaev 1969) (See Sec. 6 for further discussions on corrections to y-distortion). For relativistic electrons, with a Lorentz factor γ , a photon with energy ϵ gets boosted to $\gamma^2\epsilon$. In this case, the spectral distortion shape will be a function of the electron energy distribution. The intensity of the CMB spectrum per frequency is given by,

$$I_\nu(x) = 2 \frac{(k_B T_{\text{CMB}})^3}{(hc)^2} \frac{x^3}{e^x - 1} = I_0 I(x), \quad (9)$$

where $I(x) = \frac{x^3}{e^x - 1}$, $I(x)$ is the dimensionless intensity, x is the dimensional frequency which is given by $x = \frac{E_\gamma}{k_B T_{\text{CMB}}}$, where E_γ is the energy of photon, k_B is the Boltzmann constant, T_{CMB} is the CMB temperature, and other symbols have usual meanings. The intensity of distorted CMB spectrum is independent of redshift for a given population of electrons. The CMB distortion in the optically thin limit can be written as (Zeldovich & Sunyaev 1969; Birkinshaw 1999),

$$\Delta I(x) = (j(x) - i(x))\tau, \quad (10)$$

where $j(x)$ is the spectral intensity of photons at frequency x after being upscattered while $i(x)$ is the intensity of photons at frequency x before upscattering, $\tau = \sigma_T \int n_e dl$ where n_e is the electron number density and dl is the line of sight width of this electron population. $i(x)$ is non-zero over the range of x where the CMB photons are present. Eq. 10 can be recast to include a y-parameter as $\Delta I(x) = yg(x)$, where $y = \frac{\sigma_T}{m_e c^2} \int n_e k_B \tilde{T}_e dl$ with $k_B \tilde{T}_e = \frac{P_e}{n_e}$. Here \tilde{T}_e refers to a fictitious temperature scale for a non-thermal distribution to make the equations look suggestively similar to thermal SZ (more details can be found in Enßlin & Kaiser (2000)). In order to distinguish non-thermal spectral distortion shape from y-type distortion (the well known thermal SZ effect), we will refer to non-thermal distortion amplitude as y_{NT} , such that,

$$\Delta I_{\text{NT}}(x) = y_{\text{NT}} g_{\text{NT}}(x), \quad (11)$$

where $g_{\text{NT}}(x)$ is the spectral distortion function resulting from scattering of the CMB in a non-thermal population of clusters. We use the formalism of Enßlin & Kaiser (2000) to compute $g_{\text{NT}}(x)$ and we refer the reader to the paper for details. The pressure for a distribution of relativistic electrons is given by,

$$P_e = n_e \int dp f_e(p) \frac{1}{3} p v(p) m_e c, \quad (12)$$

where $f_e(p)$ is the normalized electron spectrum i.e. $\int f_e(p) dp = 1$ with electron dimensionless momentum $p = \sqrt{(\gamma^2 - 1)}$, $v = \beta c$, where γ is the Lorentz factor and β is the boost factor of energetic electrons. The number of CMB photons which get upscattered from energy x' to x is given by,

$$N(x' \rightarrow x) = P(t, p) \times 2 \frac{(k_B T_{\text{CMB}})^2}{(hc)^2} \frac{x'^2 dx'}{e^{x'} - 1}, \quad (13)$$

where $P(t, p)$ is the kernel of the inverse Compton scattering which captures the kinematics of photon scattering with the electrons with electron energy p , $t = \frac{x}{x'}$. The number of CMB photons within energy x' and $x' + dx'$ is $2 \frac{(k_B T_{\text{CMB}})^2}{(hc)^2} \frac{x'^2 dx'}{e^{x'} - 1}$ and $\int dt P(t, p) = 1$, which conserves the number of photons. The formula for $P(t, p)$ is

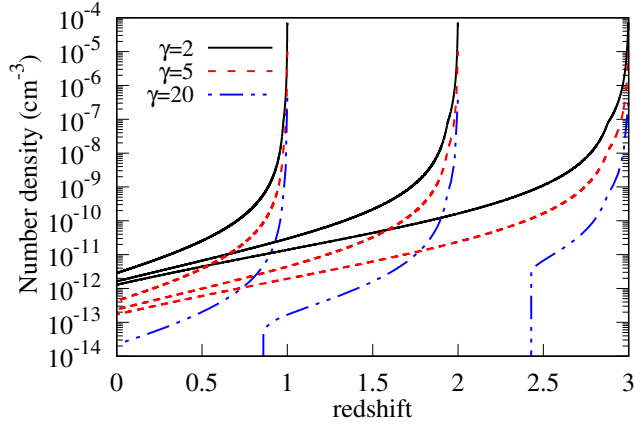


Figure 3. Differential Number density of electrons within γ and $\gamma+d\gamma$ inside a radio lobe for jets starting at different redshifts ($z = 3, 2$ & 1) for $Q_J = 10^{45}$ erg s $^{-1}$ and $t_J = 10^8$ yr. For each starting redshift, we show the results for three different energy distributions given for $\gamma = 2$ (black solid lines), 5 (red dashed lines) and 20 (blue dot-dashed lines). See text for details regarding the abrupt fall of the $\gamma=20$ curves.

given by (EnBlin & Kaiser 2000),

$$P(t; p) = \frac{-3|(1-t)|}{32p^6 t} [1 + (10 + 8p^2 + 4p^4)t + t^2] + \frac{3(1+t)}{8p^5} \left[\frac{3 + 3p^2 + p^4}{\sqrt{1+p^2}} - \frac{3 + 2p^2}{2p} (2 \operatorname{arcsinh} p - |\ln t|) \right], \quad (14)$$

The spectral intensity of upscattered photons per frequency, in frequency bin x and $x + \Delta x$, is given by,

$$j(x) = \frac{\int \int f_e(p) dp P(t, p) \frac{x'^2 dx'}{e^{x'} - 1} x}{\Delta x}. \quad (15)$$

In Fig. 2, we plot the absolute value of spectral function $g_{\text{NT}}(x)$ for power law distribution ($f_e(p) \propto p^{-\alpha_p}$) with power law index $\alpha_p=3.0$ and 2.3 . The minimum electron energy in the power law distribution is denoted by p_{min} . Higher p_{min} reduces $g_{\text{NT}}(x)$ in the CMB spectral band ($x < 10$) as CMB photons are scattered to $x > 10$ energies efficiently by energetic electrons. Decreasing α_p while keeping p_{min} fixed also reduces the magnitude of distortion in the CMB band as there are more number electrons in the higher energy tail. The value of $g_{\text{NT}}(x)$ at specific frequencies corresponding to frequency band of the upcoming Simons Observatory (Ade et al. 2019) is given in Table 1.

4 NON-THERMAL SZ SIGNAL FROM RADIO GALAXY LOBES

It is clear from the previous discussion that we need to calculate the number density of relativistic electrons as a function of the energy in order to calculate the non-thermal SZ spectrum for individual radio lobe. To proceed, we use the same strategy as used to calculate the number density of electrons which emit at 150 MHz. We divide the range in γ from 1 to 10^6 in 400 log spaced bins. Then, we use Eq. 4 and 6 for the whole range of electron energy (or γ) at each instant of time to calculate the number density $n(\gamma)d\gamma$ at that instant of time.

In Fig. 3, we plot the number density of electrons with three different instantaneous energy with jets starting at different redshifts. The

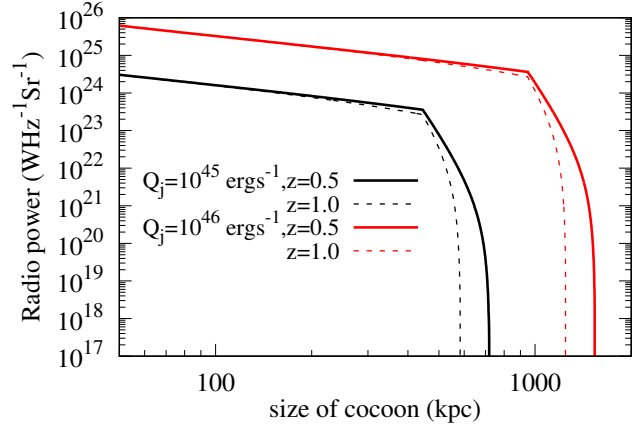


Figure 4. Radio power at 150 MHz as a function of the size of the radio lobe for a combination of jet luminosities Q_J and starting redshifts. The upper two red lines are for higher $Q_J = 10^{46}$ erg s $^{-1}$ and lower two black lines are for a lower $Q_J = 10^{45}$ erg s $^{-1}$, with solid lines corresponding to $z_{st} = 0.5$ and dashed lines for $z_{st} = 1$. The jet lifetime is $t_J = 10^8$ yr. The rapid decline in radio power is due to jet stopping and no re-acceleration of electrons.

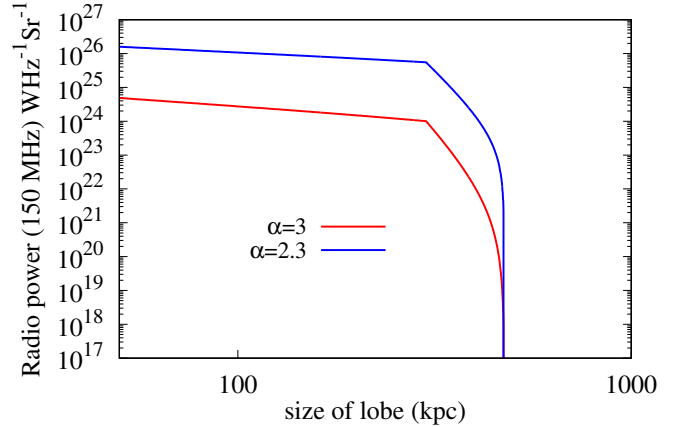


Figure 5. Radio power at 150 MHz as a function of the size of the radio lobe for $\alpha_p = 3$ and 2.3 respectively. Jet luminosity $Q_J = 10^{45}$ erg s $^{-1}$, starting redshift $z_{st} = 0.5$ and $t_J = 10^8$ yr.

lowest energy electrons dominate the total number of relativistic particles. The cooling of electrons via inverse Compton is proportional to $\gamma^2 U_C$. Therefore, at higher redshifts electrons cool much more efficiently via CMB photons. This can be clearly seen for $\gamma = 20$ curve for a jet starting at redshift 2, 3, as the electron number precipitously drops after reaching $z = 1, z = 2.5$ respectively. The efficiency of cooling of electrons is a strong function of redshift ($\propto (1+z)^4$). Therefore, the number density of electrons with the relatively higher $\gamma = 20$ falls immediately after jet the is shut off at higher redshift (e.g. for jet starting at $z=3$) while for jet starting at $z=1$, there are energetic electrons left even after the jet is shut off.

In Fig. 4, we plot the radio power as a function of size of radio lobe with different jet starting redshifts and jet luminosities keeping $t_J = 10^8$ yr. For a constant jet luminosity, radio power is independent of the initial redshift. Since we have assumed that the surrounding medium of the radio lobe has density profiles that is independent of redshift. The fall gets sharper with increasing redshift due to efficient cooling of the electrons at higher redshifts. After the jet stops, as there are no more energetic electrons that emit at 150 MHz, the power falls

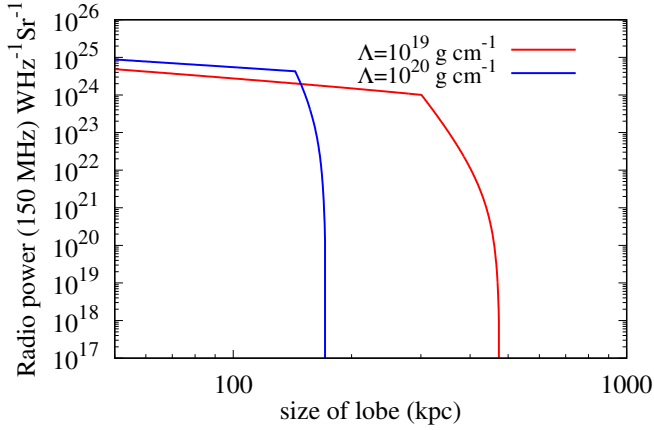


Figure 6. Radio power at 150 MHz as a function of the size of the radio lobe for different density of surrounding gas with $\Lambda = 10^{19}, 10^{20} \text{ g cm}^{-1}$ respectively. Jet luminosity $Q_J = 10^{45} \text{ erg s}^{-1}$, starting redshift $z_{st} = 0.5$ and $t_J = 10^8 \text{ yr}$.

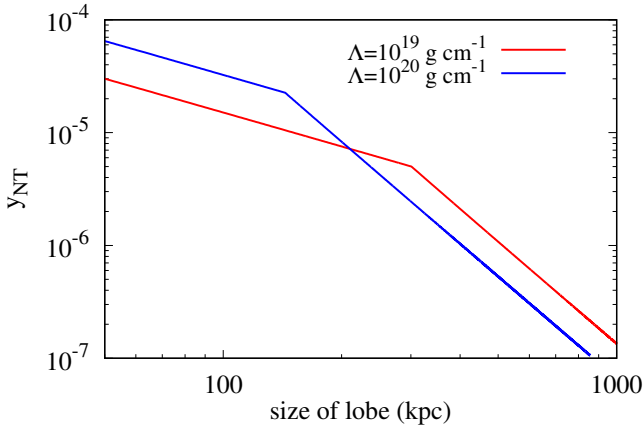


Figure 7. y_{NT} function of the size of the radio lobe for different density of surrounding gas with $\Lambda = 10^{19}, 10^{20} \text{ g cm}^{-1}$ respectively. Jet luminosity $Q_J = 10^{45} \text{ erg s}^{-1}$, starting redshift $z_{st} = 0.5$ and $t_J = 10^8 \text{ yr}$.

sharply. With increasing jet luminosity, the radio power increases as expected which is shown in Fig. 4. In Fig. 5, we compare radio power for two different spectral indices. With flatter spectral index, there is significantly higher radio power due to substantial increase of number of electrons at high energy. In Fig. 6 and 7, we compare the radio power and y_{NT} from radio galaxy lobes for different density of surrounding gas. For higher density, the lobe has a slower growth of size and therefore higher pressure for a chosen jet luminosity. Therefore, y_{rmNT} is higher for the case of higher density before the stoppage of jet. Owing to our assumption of equipartition, a smaller size of the radio lobe implies increased number density of electrons, which, in turn, implies higher magnetic energy density, leading to higher luminosity. In Fig. 8, we show y_{NT} as a function of the size of radio lobe and jet luminosity. The expression for y_{NT} is given by

$$y_{NT} = \frac{\sigma_T}{m_e c^2} p_c \times 2L_J, \quad (16)$$

where the symbols carry their usual meanings. The time taken for light to travel across the length of a radio lobe is small compared to the light travel time to reach us. Therefore, the SZ observation

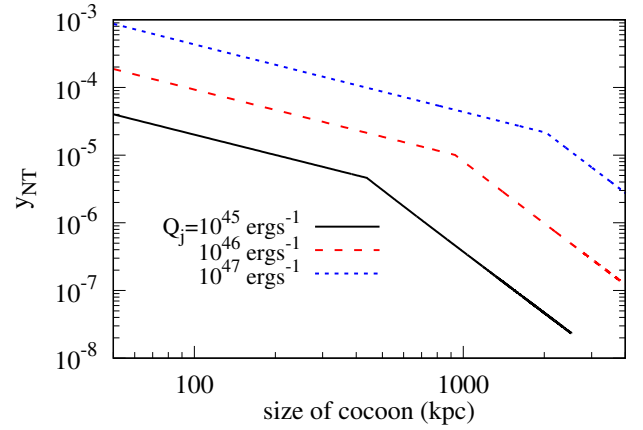


Figure 8. The non-thermal CMB distortion amplitude, y_{NT} , from radio lobes as a function of their size for different jet luminosities Q_J . In each case, the jet starting redshift is $z_{st} = 0.5$ and the jet is evolved upto $z = 0.3$. The jet lifetime is $t_J = 10^8 \text{ yr}$.

of a radio lobe gives a snapshot of the lobe during its evolution at the observed redshift. With increase in the size of the radio lobe, the pressure inside the lobe falls and, therefore, y_{NT} decreases. With increase in jet luminosity, pressure and y_{NT} increases. The curves show that in order to achieve $y_{NT} \geq 10^{-5}$, either the radio lobes have to be young (i.e. smaller in size) and the jet has to be active. In other words, it would be difficult to detect non-thermal SZ effect from ‘dead’ radio galaxies, because their distortion would be $y_{NT} \leq 10^{-6}$. Also, giant radio galaxies with Mpc size are not favourable. For a jet luminosity of $10^{46} \text{ erg s}^{-1}$ or higher, radio galaxies with size $\leq 200 \text{ kpc}$ are favourable for non-thermal SZ detection. We note that the radio lobe size depends on the ambient density and would be smaller for a radio galaxy residing in a cluster environment (see also N2010), and may provide with good targets for non-thermal SZ detection. From Fig. 8, it is interesting to note that a small young radio lobe of $L_J \sim 100 - 200 \text{ kpc}$ and $Q_J = 10^{47} \text{ erg s}^{-1}$ can have a y_{NT} equal in amplitude to thermal SZ from hot ICM of a galaxy cluster. Then taking into account the spectral distortion shape (see Fig. 13), the CMB distortion by a radio lobe inside a cluster can be a significant part of the SZ distortion from the cluster ICM. Neglecting any y_{NT} would result in a source of systematic bias for the SZ measurements towards a cluster.

5 INTERDEPENDENCY AND DEGENERACY BETWEEN PARAMETERS OF THE RADIO GALAXY EVOLUTION MODEL

In this section, we study the degeneracy between parameters of our radio galaxy evolution model. Previous discussion shows that the non-thermal SZ effect depends on the jet luminosity, the starting redshift, and the observed redshift. We scan the parameter space in jet luminosity (Q_J) and starting redshift of jet (z_{st}) which will expand to a particular size at a given redshift z . The parameter (z_{st}) can be translated to the time interval (Δt) after jet opening until the observed redshift. We consider two sources for illustrative purpose: 3C 274.1 and B2 1358+30C (Colafrancesco et al. (2013), their Table 1), observed at $z = 0.422$ and 0.206 respectively. The size of their major axis are 460 kpc and 1400 kpc respectively. We require that the radio galaxy lobe starting at $z_{st} > z$ with some Q_J will grow to size ($2L_J$) $460 \pm 10 \text{ kpc}$ and $1400 \pm 10 \text{ kpc}$ by $z = 0.422$ and 0.206

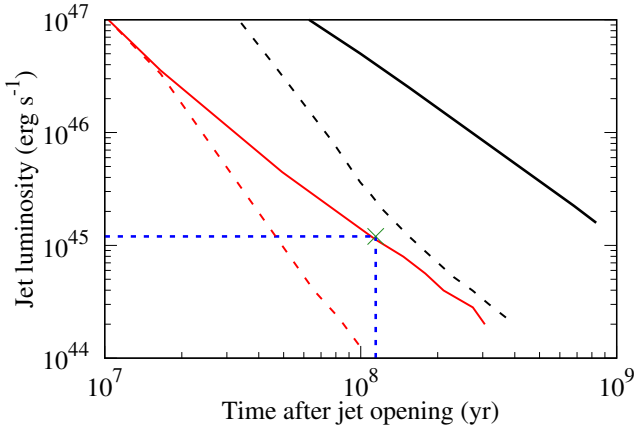


Figure 9. Modelling the jet luminosity as a function of jet starting redshifts (or equivalently time elapsed) for two sources selected from Table 2. The evolution of the radio lobes are constrained to match with observations, i.e, to reach a given observed size at a particular redshift of observation. The upper two lines are for the source B2 1358+30C with a radio lobe size of 1400 kpc with at $z = 0.206$ and the lower two lines are for the source 3C 274.1 with a radio lobe size of 460 kpc at $z = 0.422$. For each source, the solid and dashed lines are for jet lifetimes of $t_J = 10^7$ & 10^8 yr. The green cross shows that a combination of $Q_J \sim 10^{45}$ erg s $^{-1}$, $t_J = 10^7$ yr and time evolved of $\sim 10^8$ yr would model the radio galaxy lobe 3C 274.1.

respectively. We assume initial size of the lobe to be 10 kpc which is the size of a galaxy. The degeneracy between the jet luminosity and elapsed time after jet opening formation, for two different jet lifetimes, which satisfies the constraint of getting the observed radio galaxy lobe size at z is shown in Fig. 9. The luminosity is chosen to vary between 10^{44} erg s $^{-1}$ and 10^{47} erg s $^{-1}$ (Hardcastle & Croston 2020). The inferred jet luminosities from observed radio galaxies upto now seem to be below 10^{47} erg s $^{-1}$. Note that for shorter jet lifetime, luminosity has to be larger so that pressure inside the lobe is high enough to make it expand to a particular size. For Δt less than 10^7 yr, the total energy content in the radio galaxy lobe is $Q_J \Delta t$ irrespective of jet lifetime being 10^7 or 10^8 yr and, therefore, the curves with the two different lifetimes merge.

Next, we plot the degeneracies between the estimated y_{NT} and the radio power at 150 MHz in Fig. 10 for the lifetimes 10^7 yr and 10^8 yr. We take the same two sources depicted in Fig. 9. We also plot the scenario in which the radio lobe of size 1400 kpc is observed at $z=0.6$ instead $z=0.206$ and show how it is almost degenerate with the other radio lobe of size 1400 kpc, but at $z=0.206$. We have assumed electron momentum spectral index to be $\alpha_p = 3$ for the rest of the calculations as the detected radio galaxies used in this work have observed momentum spectral index ~ 3 . Compared to $\alpha_p = 2.3$, this results in a reduction of the radio power by more than an order of magnitude as electron population dies off steeply. For the range of luminosities chosen, the radio power drops drastically before the size of the lobe reaches ~ 1000 kpc for $t_J = 10^7$ yr as the jet dies off. Radio power is directly correlated with y_{NT} as the synchrotron and SZ signal comes from same population of high energy electrons assuming constant spectral index and equipartition. Higher y_{NT} corresponds to higher Q_J , and consequently, higher radio power, as more number of high energy particles are emitted by the jet.

It is interesting to note that although the pressure inside a radio lobe changes as the lobe expands, for a particular lobe size at any instant, both the radio power and y_{NT} are independent of the redshift.

This may be understood from Eq. 1. Given a particular size, since we assume the density of the surrounding medium to be independent of redshift, the pressure inside the radio galaxy lobe and, therefore y_{NT} , is independent for all redshifts. Radio power is the same once the jet lifetime is held constant and the injected particles by the jet becomes constant for all cases. For a fixed radio power, y_{NT} increases with decreasing lobe size as pressure increases with decreasing volume. For $10^7 \text{ yr} < \Delta t < 10^8 \text{ yr}$, the jet with lower lifetime stops supplying particles, which then leads to reduction in emitted radio power for the jet with $t_J=10^7$ yr compared to one with $t_J=10^8$ yr. The size of the radio lobe also makes a difference. For a given jet luminosity, the lobes can expand to 460 kpc relatively easily compared to 1400 kpc for $t_J = 10^7$ yr while the jet is still on. Therefore, a radio lobe of size 460 kpc has significant radio power for both lifetimes, $t_J=10^7$ and 10^8 yr. In contrast, for a 1400 kpc sized radio lobe, there is practically no radio power for the lower lifetime of $t_J=10^7$ yr. We conclude that selecting radio galaxy lobes of high radio power and small size (which is more likely in cluster environment, as discussed earlier) would pay off towards detection of non-thermal SZ signal.

It is interesting to consider the recent detection of non-thermal SZ signal from a radio galaxy by Malu et al. (2017) assuming it to be near the bullet cluster at $z \approx 0.3$. With this assumption, the distance of the hotspot from the radio galaxy core is estimated to be ≈ 1 Mpc. The radio power at 5.5 GHz is 4×10^{28} W, over a 2 GHz bandwidth (S. Malu, 2020, private communication). Considering the observed bandwidth, this implies radio power of 2×10^{19} W Hz $^{-1}$. Considering the angular area of the lobe to be $4' \times 4' \approx 1.35 \times 10^{-6}$ sr, and assuming the minor axis to be half the hotspot distance, as in our model, the radio power turns out to be 3×10^{25} W Hz $^{-1}$ sr $^{-1}$. Then, with a spectral index of -1 (corresponding to $\alpha_p = 3$), this implies a power at 150 MHz $\approx 5.5 \times 10^{26}$ W Hz $^{-1}$ sr $^{-1}$. This level of radio power is shown with 15 percent measurement uncertainty with a grey horizontal band in Fig. 11. In this figure, we also show the radio power as a function of y_{NT} for different jet lifetimes t_J . The jet luminosity is varied between $10^{44} - 10^{48}$ erg s $^{-1}$. In their paper, Malu et al. (2017) reported an observed non-thermal SZ distortion with $y = 2 \times 10^{-5}$. Note that in our calculation, the jet luminosity has to be slightly higher than 10^{47} erg s $^{-1}$ to explain the observed radio power for a 1 Mpc radio lobe. The radio power for a 1 Mpc lobe which can be achieved by jet luminosity 10^{47} erg s $^{-1}$ is shown as the black cross in Fig. 11. The required jet luminosity to explain the radio power turns out to be $\sim 3 \times 10^{47}$ erg s $^{-1}$. Alternatively, the radio galaxy may be a foreground object, in which case its size is smaller, and a smaller jet luminosity is needed to explain this observation. In order to determine the requirements of energetics, we fix the jet luminosity at $Q_J = 10^{47}$ erg s $^{-1}$ and vary the size of the lobe. We find that for a radio lobe with size 200 kpc, the radio power can be explained by $Q_J = 10^{47}$ erg s $^{-1}$ (shown with the magenta cross in the same figure). This foreground object has to be, then, located at $z = 0.05$ to have the observed angular size in the sky.

We would like to point out that Malu et al. (2017) assumed non-relativistic distortion in obtaining their value of $y = 2 \times 10^{-5}$. However, one actually measures ΔI_ν , which can be written as,

$$\begin{aligned} \Delta I_\nu(x) &= y g_T(x) && \text{(Malu et.al. (2017))} \\ &= y_{NT} g_{NT}(x) && \text{(this work),} \end{aligned} \quad (17)$$

where y and $g_T(x)$ is the non-relativistic y -distortion and the spectrum respectively, and similarly y_{NT} and $g_{NT}(x)$ for non-thermal distortions. Therefore, there is a degeneracy between y_{NT} and $g_{NT}(x)$ (or p_{min}) for a given $\Delta I_\nu(x)$. This is true for the measurement of $\Delta I_\nu(x)$ at a single frequency which was the case for the reported detection at 18 GHz. The magnitude of $g_{NT}(x)$ is lower than $g_T(x)$

for all x (see Fig. 6 of (Enßlin & Kaiser 2000)) and this difference depends sensitively on the value of p_{\min} . At $x = 0.35$ (corresponding to frequency 18 GHz), the value of $g_{\text{T}} = 0.24$ while $g_{\text{NT}} = 0.1$ and 0.03 for $p_{\min} = 1$ and 2 respectively (as seen in Fig. 2). Therefore, for $p_{\min} = 1$ and 2, y_{NT} is higher than $y = 2 \times 10^{-5}$ by a factor of 2.5 and 10 respectively, and can easily reach $y_{\text{NT}} = 2 \times 10^{-4}$ for $p_{\min} = 2$.

The degeneracy between y_{NT} and p_{\min} was already noted in Malu et al. (2017) (their Fig. 2). They obtain an upper limit on p_{\min} between 5 to 10 using X-ray constraints. Note, that their y -value is for non-relativistic SZ where the electron spectrum (p_{\min}) does not enter. Moreover, without a radio galaxy evolution model, they could not relate y -value to the size of the radio galaxy lobe. In contrast, our approach of using a detailed radio galaxy evolution model leads us to predict a value of y_{NT} for a given size of the radio lobe and radio power. From our model, y_{NT} for 1 Mpc object turns out to be $6 - 7 \times 10^{-5}$ (corresponding to jet luminosity of $\sim 3 \times 10^{47}$ erg s^{-1}). This value of y_{NT} is consistent with the value of $p_{\min} = 1$. Even if we mistake the source to be a foreground object of size 200 kpc, the obtained value of y_{NT} from our evolutionary model is $\sim 2 \times 10^{-4}$ which is consistent with $p_{\min} = 2$. The increase in y_{NT} for 200 kpc lobe as compared to 1 Mpc size lobe necessarily leads to increase in p_{\min} (or decrease in value of $g_{\text{NT}}(x)$ at $x = 0.35$) such that $\Delta I_{\nu}(x)$ is unchanged as in Eq. 17. Note, that irrespective of the degeneracy between y_{NT} and p_{\min} , an arbitrary increase in y_{NT} in our radio galaxy evolutionary model would require high non-thermal pressure which necessarily requires the size of the radio lobe to be unrealistically small for a given radio luminosity. Therefore, the observed radio power and size of the radio lobe (assuming the lobe to be at $z \sim 0.3$) is consistent with $y_{\text{NT}} = 6 - 7 \times 10^{-5}$ which requires $p_{\min} \sim 1$. This is the first estimate of the lower energy cutoff of non-thermal electron population in radio galaxy lobe using SZ effect. In Fig. 12, we repeat the above calculation but with a flatter spectral index $\alpha_p = 2.3$. We find that for $t_j \sim 10^7$ yr, our model predicts $y_{\text{NT}} \sim 2 \times 10^{-5}$ but with jet luminosity higher than 10^{47} erg s^{-1} . But to explain Malu et al. (2017) result, y_{NT} has to be $\sim 10^{-4}$ as $g_{\text{NT}}(x)$ at $x = 0.35$ is ~ 0.05 for the spectral index chosen. Therefore, our galaxy evolution model is inconsistent with a spectral index of 2.3. We also note that this object is at a sufficiently low redshift, for which our assumption of the ambient density is reasonable.

If we have measurements of the CMB distortions at multiple frequencies, we can directly measure the value of p_{\min} from the shape of distortion and break the degeneracy between y_{NT} and $g_{\text{NT}}(x)$. The viability of such measurements with upcoming CMB experiments is discussed in Sec. 6.

5.1 Comparison with Colafrancesco et. al.

We compare our non-thermal SZ calculation with the radio galaxies listed in Colafrancesco et al. (2013). The authors assumed a static electron distribution where the electron number density is given by,

$$N_e(p, r) = k_0 g_e(r) A(p_1, p_2, \alpha_p) p^{-\alpha_p}, \quad (18)$$

The value of k_0 is fixed to be 2.6 cm^{-3} and the average value of observed $\alpha_p = 3$ which is obtained from fitting data to radio and X-ray observations. The electron number density is assumed to be constant, so that $g_e(r) = 1$. A is a normalizing constant such that $\int_{p_1}^{p_2} A p^{-\alpha_p} = 1$. p_1 is fixed to be 1. This can be converted to cutoff in γ as $\gamma = \sqrt{1 + p_1^2}$. The size of galaxy is assumed to be ellipsoidal with major and minor axis as given in Table 1. The line of sight

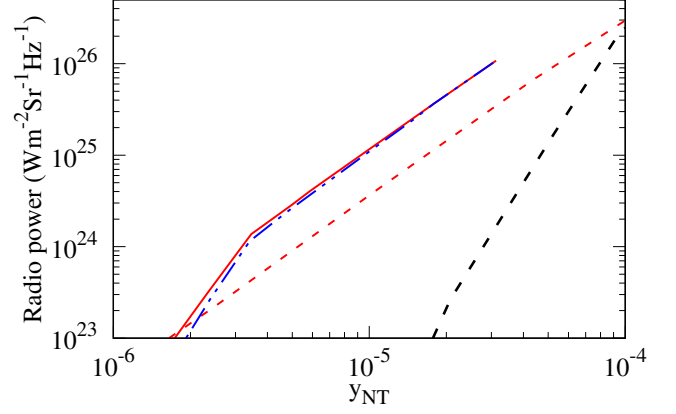


Figure 10. y_{NT} vs radio power at 150 MHz for two sources selected from Table 2. The evolution of the radio lobes are constrained to match with observations, i.e., to reach a given observed size at a particular redshift of observation. The dashed lines are for the source 3C 274.1 having radio lobe size of 460 kpc at $z = 0.422$, with the black thick dashed line for jet lifetime $t_j = 10^7$ yr and thin red dashed line for $t_j = 10^8$ yr. The other source, B2 1358+30C, having size of 1400 kpc at $z = 0.206$, is shown with the red solid line. Note, that B2 1358+30C would have been almost degenerate in y_{NT} -radio power plane with a source of size 1400 kpc at $z = 0.6$ & $t_j = 10^8$ yr, shown with the blue dot-dashed line.

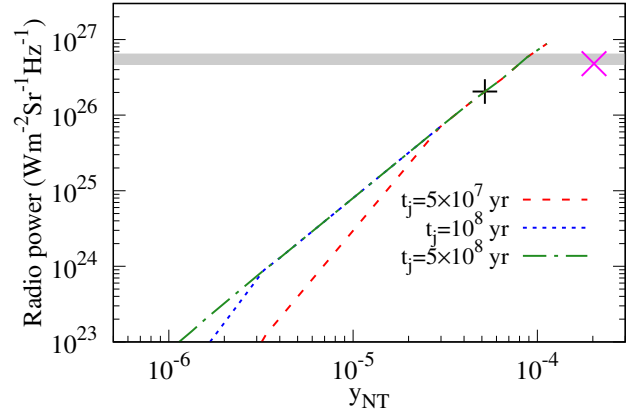


Figure 11. Similar to Fig. 10, y_{NT} vs radio power at 150 MHz for radio lobes constrained to have size $2L_j = 1$ Mpc at $z_{\text{obs}} = 0.3$ (to model the source observed by Malu et al. (2017)) for different jet lifetimes. The jet luminosity is varied between $10^{44} - 10^{48}$ erg s^{-1} . The grey horizontal band shows the radio power observed by Malu et al. (2017). The black cross corresponds to the radio luminosity and y_{NT} which can be achieved for a 1 Mpc lobe with a Q_j of 10^{47} erg s^{-1} . In contrast, for the radio lobe being closer to us (i.e., having a lower z , see text for details) such that the size is 200 kpc, but with the same Q_j , the corresponding point is shown by the magenta cross which touches the grey band.

is assumed to be the major axis. From these information one can calculate the optical depth for CMB photons.

In Table 2, we list the sources, their size, radio power at 150 GHz which were considered in Colafrancesco et al. (2013). We then predict the y_{NT} , an estimate of t_j and flux density for Simons Observatory at two frequencies, which are allowed by our model and satisfy the size and radio flux density as given. The beam and instrument noise for Simons Observatory are listed in Table 1 of Ade et al. (2019). We use the best case scenario with specifications for LAT ($f_{\text{sky}} = 0.4$) with

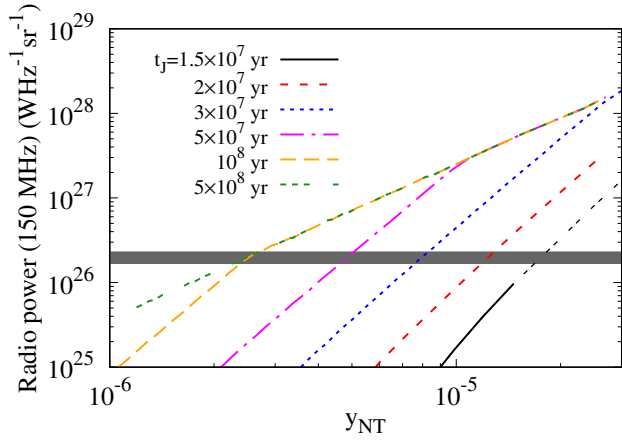


Figure 12. Same calculations as in Fig. 11 but with $\alpha_p = 2.3$. The jet luminosity is varied between $10^{44} - 10^{47} \text{ erg s}^{-1}$ except for the thin dashed black line for which the highest jet luminosity is chosen to be $10^{48} \text{ erg s}^{-1}$

FWHM as the beam. The expected noise are 6.3 and $37 \mu\text{K-arcmin}$ for the two frequencies in Table 2. The t_j values listed in Table 2 should be considered as a lower limit of jet lifetime that satisfies the constraints. We see that for most of the sources, the required jet luminosity needs to be higher than $10^{47} \text{ erg s}^{-1}$. Therefore, we have allowed the jet luminosity to vary between 10^{44} and $10^{48} \text{ erg s}^{-1}$. For a given radio galaxy size, there is a three-way degeneracy between the jet luminosity, the lifetime of jet and the starting redshift of jet (z_{st}) or the time-interval between jet starting redshift and observed redshift (Δt) (Fig. 9). For a given jet lifetime and size, we can increase Δt by reducing jet luminosity or vice versa. Therefore, a bound on jet luminosity gives a bound on Δt . The radio power from a galaxy drops sharply once jet is off i.e. we should not observe radio flux density if $\Delta t > t_j$. This criteria and prior condition on jet luminosity gives a lower bound on t_j . However, radio observation does not give an upper bound on t_j since the radio lobes becomes invisible in radio as it grows too big and faint. In contrast, the radio galaxy should be observable in SZ even after jet goes off. Therefore, SZ observations can put an upper bound on jet lifetimes of these radio galaxies. In Table 3, we show the predicted y_{NT} and lower estimate of t_j assuming the spectral index of electron distribution to be 2.3. For this case, the predicted y_{NT} are orders of magnitude lesser compared to the case when the index is 3. This can be understood from the discussion of Fig. 5. For same jet luminosity, the radio power from an electron distribution with flatter spectral index is higher compared to a steeper spectrum. Therefore, to explain a given radio power, the inferred jet luminosity is smaller in case of flatter spectral index and hence smaller pressure inside the lobe and smaller y_{NT} .

6 DETECTION PROSPECTS OF NON-THERMAL SZ WITH FUTURE CMB EXPERIMENTS

In this section, we study the feasibility of detecting non-thermal SZ with future CMB experiments. The distortion in intensity I_ν of CMB at a frequency ν and towards a localized concentration of hot electrons can be written as,

$$\Delta I_\nu = \Delta I_y + \Delta I_\mu + \Delta I_{kSZ} + \Delta I_{rSZ} + \Delta I_{NT}, \quad (19)$$

where ΔI_y is the typically dominant non-relativistic y distortion, ΔI_μ is the μ distortion, ΔI_{kSZ} is the temperature shift of the CMB black body due to kSZ effect (Sunyaev & Zeldovich 1980), ΔI_{rSZ} is the

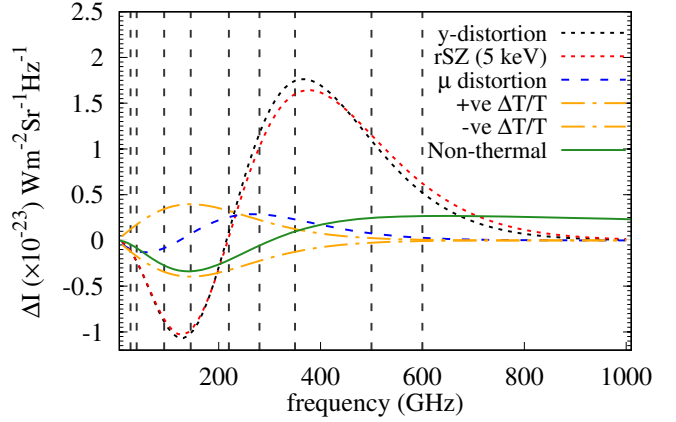


Figure 13. The frequency dependence of various possible distortions from CMB black body including the non-thermal SZ distortion (green solid line). The amplitude of distortion is chosen to be 10^{-6} for each type. Moreover, for the non-thermal spectrum, we choose $p_{\min} = 1$. The vertical dashed grey lines correspond to current and upcoming CMB observational frequencies.

relativistic SZ signal from a massive galaxy cluster and ΔI_{NT} is the non-thermal SZ distortion. The expression for ΔI_y , ΔI_μ and ΔI_{kSZ} are given by (Zeldovich & Sunyaev 1969; Sunyaev & Zeldovich 1970; Illarionov & Siuniaeiv 1975),

$$\Delta I_y = y \frac{2h\nu^3}{c^2} \frac{xe^x}{(e^x - 1)^2} \left[x \frac{e^x + 1}{e^x - 1} - 4 \right] \quad (20)$$

$$\Delta I_\mu = \mu \frac{2h\nu^3}{c^2} \frac{e^x}{(e^x - 1)^2} \left[\frac{x}{2.19} - 1 \right] \quad (21)$$

$$\Delta I_{kSZ} = \left(\frac{\Delta T}{T} \right) \frac{2h\nu^3}{c^2} \frac{e^x}{(e^x - 1)^2} \quad (22)$$

The y -distortion can have contribution from both pre-recombination universe as well as post-recombination universe while μ -distortion can only be created at redshifts greater than 2×10^5 . The SZ spectrum from electrons with energy $\gtrsim \text{keV}$ is obtained by including Klein-Nishina corrections for Compton scattering which can be calculated perturbatively as an expansion in $\frac{T_e}{m_e}$ (Itoh et al. 1998; Challinor & Lasenby 1998; Sazonov & Sunyaev 1998; Dolgov et al. 2001). For example, The temperature of massive galaxy cluster with mass 10^{14} times solar mass can be $\sim 5 \text{ keV}$ (Erlanger et al. 2018), and with a typical $y \sim 10^{-5}$.

The unique spectral shapes of the different SZ distortions can be used to separate them, hence isolating the non-thermal SZ from other dominant CMB fluctuations, at relevant angular scales. In Fig. 13, we plot the intensity of different distortions as discussed above. The spectral shapes of these distortions are different from each other. Therefore, with a multifrequency study, we can distinguish non-thermal distortion from other forms of distortions. To check if non-thermal distortion can be mimicked by combination of other distortions, we find the best fit to non-thermal distortion shape from a linear combination of y , μ , kSZ and rSZ distortions i.e. we want to write ΔI_{NT} as,

$$\Delta I_{NT} = y\Delta I_y + \mu\Delta I_\mu + \left(\frac{\Delta T}{T} \right) \Delta I_{kSZ} + y_{rSZ}\Delta I_{rSZ}, \quad (23)$$

where y , μ , $\frac{\Delta T}{T}$ and y_{rSZ} are the best fit parameters. The basic idea is that if the non-thermal distortions cannot be written as a linear

source	z	angular size arcsec (major axis)	size kpc	Flux mJy	y_{NT}	t_j yr	flux (μ K-arcmin) (150 GHz)	flux (μ K-arcmin) (280 GHz)
CGCG 186-048	0.063	388	485	1	2×10^{-5}	5×10^7	399 (63σ)	6.1 (1.6σ)
B2 1158+35	0.55	70	462	1.3	2×10^{-4}	5×10^7	130 (21σ)	20 (0.5σ)
3C 270	0.0075	577	93	113	1×10^{-5}	10^7	441 (70σ)	68 (1.8σ)
87GB 121815.5+..	0.2	924	3141	0.43	1×10^{-5}	10^8	1131 (180σ)	174 (4.7σ)
3C 274.1	0.422	89	508	30	6×10^{-4}	5×10^7	630 (100σ)	174 (2.6σ)
4C +69.15	0.106	822	1646	26	1×10^{-4}	5×10^7	8956 (1421σ)	1378 (37σ)
3C 292	0.71	64	473	16	8×10^{-4}	5×10^7	434 (69σ)	67 (1.8σ)
B2 1358+30C	0.206	408	1421	0.28	2×10^{-5}	10^8	441 (70σ)	68 (1.8σ)
3C 294	1.779	29	253	2	4×10^{-4}	10^7	45 (7σ)	7 (0.2σ)
PKS 1514+00	0.052	519	543	480	5×10^{-4}	5×10^7	17851 (2833σ)	2746 (74σ)
GB1 1519+512	0.37	312	1646	22	3×10^{-4}	10^8	3871 (614σ)	595 (16σ)
3C 326	0.0895	684	1177	22	10^{-4}	10^8	6201 (984σ)	954 (26σ)
7C 1602+3739	0.814	100	778	0.33	10^{-4}	5×10^7	132 (21σ)	20 (0.5σ)
MRK 1498	0.0547	583	639	15	2×10^{-4}	5×10^7	9010 (1430σ)	1386 (37σ)
B3 1636+418	0.867	57	452	16	10^{-4}	5×10^7	43 (6.8σ)	7 (0.2σ)
Hercules A	0.154	200	551	253	9×10^{-4}	5×10^7	4772 (750σ)	734 (20σ)
B3 1701+423	0.476	120	735	1.1	10^{-4}	5×10^7	191 (30σ)	29 (0.8σ)
4C 34.47	0.206	92	320	9.5	3×10^{-4}	5×10^7	337 (53σ)	52 (1.5σ)
87GB 183438.3+..	0.5194	69	443	3.9	3×10^{-4}	5×10^7	190 (30σ)	29 (0.8σ)
4C +74.26	0.104	773	1522	94	3×10^{-4}	5×10^7	23760 (3771σ)	3655 (99σ)
RG01 (Malu et al. 2017)	0.3	240	1100	7×10^{-5}	2700	10^8	534 (85σ)	82.2 (2.2σ)

Table 2. We list the redshifts of the sources, size (major axis), radio flux density at 150 GHz given in Table 1 and 2 of (Colafrancesco et al. 2013). We predict the corresponding y_{NT} , t_j and flux density for the source with Simons Observatory (Ade et al. 2019) or CMB-S4 (Abazajian et al. 2019) type experiment to match the observation of size and radio power, allowed by our model for radio galaxy. We have used the best case noise limit (LAT, $f_{sky} = 0.4$) of Simons Observatory to derive the significance of the detection. For non-thermal spectrum, we choose $p_{min} = 1$. We have abbreviated a couple of source names to make space. Please note that for radio galaxy RG01, the flux density is given at 5.5 GHz. We also assume the source to be at $z=0.3$ (at the location of bullet cluster). If the source is a foreground object, then the physical properties of the galaxy will be different (see text).

source	y_{NT}	t_j yr
CGCG 186-048	3×10^{-7}	3×10^8
B2 1158+35	2×10^{-6}	2×10^8
3C 270	6×10^{-7}	10^8
87GB 121815.5+..	3×10^{-7}	5×10^8
3C 274.1	8×10^{-6}	10^8
4C +69.15	2×10^{-6}	10^8
3C 292	7×10^{-6}	10^8
B2 1358+30C	3×10^{-7}	5×10^8
3C 294	9×10^{-7}	5×10^7
PKS 1514+00	4×10^{-6}	10^8
GB1 1519+512	5×10^{-6}	10^8
3C 326	10^{-6}	2×10^8
7C 1602+3739	10^{-6}	3×10^8
MRK 1498	6×10^{-7}	3×10^8
B3 1636+418	10^{-6}	3×10^8
Hercules A	9×10^{-6}	10^8
B3 1701+423	9×10^{-7}	2×10^8
4C 34.47	2×10^{-6}	10^8
87GB 183438.3+..	3×10^{-6}	10^8
4C +74.26	2×10^{-6}	2×10^8

Table 3. Same as Table 2 but with a flatter spectral index $\alpha_p = 2.3$. We only show the predicted y_{NT} and estimated lower estimate of t_j .

combination of other forms of distortions i.e. if there is a non-zero residual after the best fit has been removed from total distortion, then we can detect the non-thermal part of the total distortion as the residuals of total distortion signal.

In Fig. 14, we plot the best fit with six frequency channels of Simons Observatory which will start observation in near future. For the unconstrained best fit, the best fit parameter of y , y_{rSZ} , μ and $\Delta T/T$ can have positive and negative sign. With these unconstrained parameters, we have a very good fit to non-thermal distortion. Note

that even in the absence of a galaxy cluster, the y and μ -type distortion can be created in pre-recombination universe from acoustic damping, baryon cooling or injection of electromagnetic energy from decay or annihilation of unstable particles etc. (Chluba & Sunyaev 2012; Khatri et al. 2012; Chluba et al. 2012). While acoustic damping and injection of energy can give rise to positive y or μ -type distortion, baryon cooling gives rise to negative μ distortion of the order $10^{-8} - 10^{-9}$. In post recombination universe, the hotter electrons in the structures boost CMB photons to higher energy. Therefore, it is

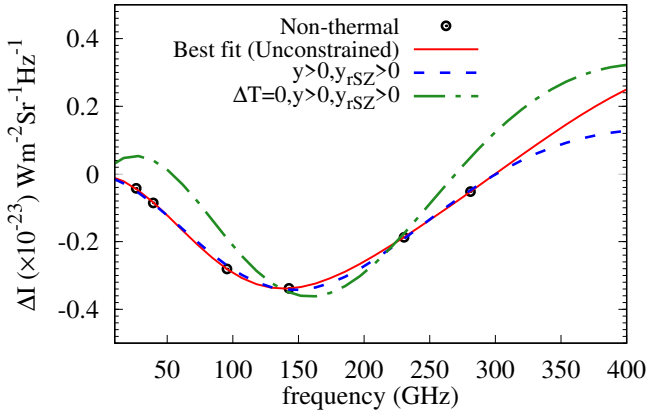


Figure 14. The intensity of non-thermal distortions at frequencies 27, 39, 93, 145, 225 and 280 GHz as proposed for the upcoming Simons Observatory (shown with open circles), having the amplitude $y_{\text{NT}} = 10^{-6}$. The best fit to non-thermal distortion using a linear combination of y , μ , kSZ and rSZ distortions is shown by the solid red line, which perfectly passes through the observed points. The unconstrained fit is shown by red-solid line whereas constraints on the amplitude of thermal SZ results in the blue dashed line and an additional constraint of no kinematic SZ gives the green dot-dashed line.

reasonable to assume that y and y_{rSZ} should be positive while the kSZ temperature shift can be positive and negative as this distortion is produced by moving electrons. With the constraints that y and $y_{\text{rSZ}} > 0$, we can still manage to have a very good fit to non-thermal spectrum in the frequency range 20-300 GHz. Note that, a negative kSZ temperature shift can mimic non-thermal SZ spectrum by shifting the null point to higher frequencies. As can be seen from Fig. 13, the shape of a negative kSZ is roughly similar to non-thermal distortion for frequency $\lesssim 300$ GHz. Once, we ignore kSZ with the positivity condition on y and y_{rSZ} , we are able to distinguish non-thermal SZ signal as there are non-zero residual at some frequencies (Fig. 16). For an order of magnitude estimate of temperature shift due to kSZ, we consider the source Hercules A from Table 2 with highest y_{NT} parameter ($y_{\text{NT}} = 9 \times 10^{-6}$). The optical depth of this source turns out to be $\sim 10^{-4}$. With $v/c \sim 10^{-3}$, we see that the distortion due to kSZ are of the order $\frac{v}{c}\tau \sim 10^{-7} - 10^{-6}$. In the above estimate, we have assumed that the positive and negative kSZ contribution from the jet would cancel and only the virial velocity of cluster will contribute to the kSZ signal. For a spherical source, there is full cancellation. For non-spherical source, there can be a small effect due to incomplete cancellation. However, the more the inclination, the kSZ is also low because the component of radial velocity is smaller (see Aghanim et al. (1996) and Majumdar et al. (2001) as example). Therefore, we can safely ignore the kSZ temperature shift and consequently will be able to differentiate non-thermal SZ from other distortions, for this source.

For a completely unambiguous detection without any assumption on the y , μ , kSZ and rSZ distortions, it is clear from the above discussion that the location of the null point of the total distortion may not be a reliable signature of non-thermal SZ from future CMB experiments. However, as can be seen from Fig. 13, the intensity of y , μ , kSZ and rSZ distortions after 400 GHz starts to decrease in magnitude and approach zero while for non-thermal SZ, the spectrum is relatively flat. Therefore, high frequency channels (> 400 GHz) would be able to differentiate non-thermal distortion from others. We design a hypothetical experiment with all the frequency band of Simons Observatory and add three more frequency channel at 350

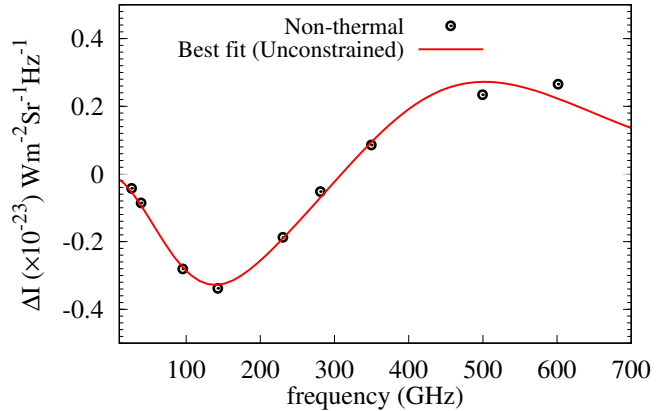


Figure 15. Same as Fig. 14, but for a hypothetical experiment with the six frequencies of Simons observatory and additional frequency bands at 350 GHz, 500 GHz and 600 GHz. A linear combination of y , μ , kSZ and rSZ distortions can no more pass through all the observed points.

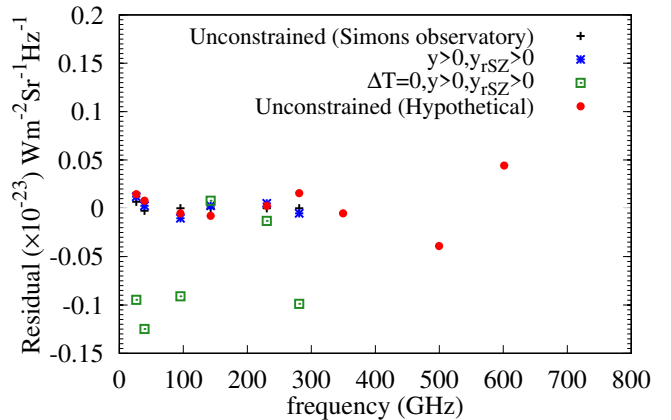


Figure 16. Residual after subtracting best fit linear combination of y , μ , kSZ and rSZ distortions from non-thermal distortions corresponding to Figs. 14 & 15.

GHz, 500 GHz and 600 GHz. In this setup, we are able to distinguish non-thermal distortion from others without putting any constraints on best fit parameters of y , μ , temperature shift due to kSZ and rSZ distortions as can be clearly seen in Fig. 15 and Fig. 16.

Some of the sources listed in Table 2 can be very good candidates for Simons Observatory or CMB-S4 experiments due to high signal to noise ratio at 150 and 280 GHz frequency bands. However, for unambiguous detection, we will need higher frequency bands. Experiments like Probe of Inflation and Cosmic Origins (PICO) (Hanany et al. 2019) with many more frequency bands with noise $\sim O(1)$ $\mu\text{K-arcmin}$ upto 500 GHz will be extremely useful for such detections. We need to also take into account the effect of CMB primordial fluctuations, internal motions and calibration etc for such detections. However, these details are beyond the scope of this paper.

7 DISCUSSION

For the sake of simplicity, we have assumed a constant value of the ambient density in our radio galaxy evolutionary model. Realistically, the density increases with redshift, since it should scale with the

critical density, thus implying smaller sized of radio galaxy lobes and higher radio power at larger redshifts, but also with rapid decline in radio power once the jet switches off. The net non-thermal SZ signal will be larger. Note, that for particular radio galaxies considered in this work (refer to Table 2), the estimates of radio power and y_{NT} will not differ significantly from those presented here.

The SZ effect from galaxy clusters can be used as cluster mass proxy in SZ surveys which aims at using cluster number counts and their spatial correlations to constrain cosmological parameters. However, this is crucially dependent on establishing an unbiased SZ distortion - cluster mass scaling. The thermal SZ effect y -distortion is the dominant distortion for large clusters ($y \sim 10^{-5} - 10^{-4}$ for clusters of virial mass $\sim 10^{14} M_{\odot} - 10^{15} M_{\odot}$). The non-thermal SZ signal from radio lobes inside the clusters can easily be a significant fraction of the thermal SZ from the cluster gas and cannot not be ignored. In the absence of observations at many different frequencies, one needs to model the non-thermal SZ (as in Table 2) and subtract it out from the total SZ distortion so as to have an unbiased estimate of the SZ from the cluster gas. However, if there are many observable frequencies, then the separation of the different components can be done by utilizing their unique spectral shapes as demonstrated in the previous section. Additionally, neglecting SZ distortions from radio lobes (inside clusters) would be bias the estimate of the Hubble Constant H_0 using a combination of SZ and XRay observations towards galaxy clusters. It is interesting to note that subtracting a contribution from radio lobes lowers the estimate of the net SZ distortion from the cluster gas, and pushes the the value of H_0 up, in the right direction.

Other than radio galaxy lobes residing within clusters, radio galaxies having radio lobes are ubiquitous in our Universe. In the previous sections, we have calculated the magnitude of distortion of the CMB spectrum from individual radio galaxy lobes. As a next step, we can consider an ensemble of radio lobes populating the universe and calculate the global averaged CMB distortions. A first calculation of the average y -distortion has been done in Yamada et al. (1999) and Majumdar (2001) assuming that the radio galaxy lobes reside inside the dark matter halos with one-percent halo occupational efficiency. The jet luminosity was assumed to be equal to the Eddington luminosity of central black hole of mass M_{BH} with $M_{\text{BH}} = 0.002 M_{\text{halo}}$. Moreover, Majumdar (2001) calculated the angular power spectrum, C_{ℓ} , of CMB distortions from unresolved radio galaxy lobes. However, these initial efforts assumed the distortion to be non-relativistic y -distortion and concluded that a cosmological distribution of radio lobes with $t_{\text{J}}=10^7$ yr to be severely constrained due to the COBE CMB spectral distortion limit (Fixsen et al. 1996). Our calculations suggest that in a Λ CDM universe with the current cosmological parameters, the global averaged $\langle y \rangle \sim 10^{-6}$ for $t_{\text{J}} = 10^7$ yr. Several improvements are in order to make progress - for example, the assumed jet luminosity of their model may be too high compared to the jet luminosity inferred from individual radio galaxies (Hardcastle & Croston 2020). Also, the efficiency factor will not be a constant but a function of dark matter halo mass. Our preliminary work on calculating the two point correlation functions of SZ fluctuations imply that the contribution from radio galaxies can be ~ 10 percent of contribution from galaxy clusters. We will present the results for $\langle y \rangle$ and C_{ℓ} for a cosmological distribution of radio galaxy lobes in a followup work.

8 CONCLUSIONS

We perform a detailed quantitative study of the non-thermal hot electrons in radio galaxy lobes, both during the lifetime of the radio

jets and after the jets stop, as a potential source of non-thermal SZ distortion to CMB black body spectrum. Since the energetic particles inside the radio lobes cool via both synchrotron radiation and inverse Compton scattering, there is a correlation between emitted radio power and expected intensity of CMB distortion at any instant. Combining radio galaxy evolution models of Kaiser et al. (1997) with suitable modification for jet stopping as in Nath (2010), we are able to estimate the physical properties of the radio lobes at any instant of time.

We predict the value of y_{NT} , given the observed size and radio power of a galaxy lobe, from our evolutionary model by taking into account the cooling of electrons of all energy. This is in contrast to previous works, for example Colafrancesco et al. (2013), in which the authors inferred the value of number density of electrons from radio and X-ray observations. X-ray allows one to probe only a portion of the electron spectrum, whereas SZE, being dependent on the total energy density of electrons, can provide a better diagnostic of the electron spectrum. The lack of Faraday rotation from these galaxies can be due to deviation from equipartition, and may not directly tell us about p_{min} . Radio and X-ray observation constrain the spectrum of electrons at $\gamma > 10^4$. The authors extrapolate the spectrum of electrons to lower energy electrons which are responsible for the SZ signal. We do no such extrapolation. Further, we use the non-thermal spectrum of these relativistic particles to calculate the distortion on the CMB for a given size and radio power of the radio galaxy lobe. A summary of our predictions for 21 radio galaxy lobes is tabulated in Table 2. The key points of this work are summarized below :

- Although the pressure inside a radio lobe changes as the lobe expands, for a particular lobe size at any instant, both the radio power and y_{NT} is independent of redshift. This is a consequence of assuming the density of the surrounding medium to be independent of the redshift. As long as jet is turned on, radio power is just a function of the jet luminosity and not the jet lifetime i.e. the radio power from two sources with $t_{\text{J}} = 10^7$ and 10^8 yr are the same when both sources are relatively young.
- The injected electrons, when the jet is on, cool efficiently via inverse Compton scattering especially at higher redshifts. After the jet shuts off, there is no more supply of energetic electrons. Therefore, as soon as the jet turns off, there is a steep fall of radio power as the energetic electrons which are responsible for radio emission have all cooled down.
- For a fixed radio power, y_{NT} increases with decreasing radio lobe size as pressure is larger for smaller volume (which leads to the expansion of the radio lobes). The prospect of detecting non-thermal SZ from radio lobes increases if the radio lobes are young (or smaller in size) and/or jet the is active.
- A direct consequence of the above points is that radio galaxy lobes residing in cluster environments would be better potential targets for non-thermal SZ detection. Similarly, dead field radio galaxies, with large radio lobe sizes, are not favourable sources for non-thermal SZ detection.
- The analysis presented in this paper can successfully model the recent first detection of non-thermal SZ effect from the radio galaxy RG01 (Malu et al. 2017). This gives us the confidence in predicting the non-thermal SZ distortion for a further sample of 20 radio galaxy sources (in Table 2) which can be targeted by upcoming ground based SZ searches.
- For a given intensity of distortion on the CMB, there is a degeneracy between y_{NT} and $g_{\text{NT}}(x)$. In contrast to previous studies, we can predict y_{NT} from our galaxy evolution model which can then constrain the value of spectral function $g_{\text{NT}}(x)$.

• Radio and SZ detection of radio lobes can help determine the physical properties of energetic electrons inside the radio galaxy lobes. For the non-thermal SZ detection from RG01, we are able to constrain the value of p_{\min} (the lowest energy threshold of the electron spectrum) using SZ effect for the very first time. We find $p_{\min} \sim 1 - 2$ is needed to explain the observations.

• We demonstrate that future CMB experiments, with higher frequency bands (≥ 300 GHz), are needed for differentiating non-thermal SZ from radio lobes from other SZ distortions (for example, kSZ distortions from clusters of galaxies). In this respect CMB S4 (Abazajian et al. 2016), PICO (Hanany et al. 2019), CMB Bharat (CMB Bharat Consortium, Exploring Cosmic History and Origin 2018) would be most promising.

ACKNOWLEDGEMENTS

We acknowledge the use of computational facilities of Department of Theoretical Physics at Tata Institute of Fundamental Research, Mumbai. We acknowledge support of the Department of Atomic Energy, Government of India, under project no. 12-R&D-TFR-5.02-0200. SKA is grateful for financial support from the Royal Society and Prof. Jens Chluba for the invitation to University of Manchester, during which a part of this work was done. BN wishes to thank Siddharth Malu for useful discussions. SM wishes to use this opportunity to recollect the very fond memory of his first meeting with late Sergio Colafrancesco when SM was an PhD student on his first trip outside his country and Sergio had driven his car to Roma Termini station to pick up SM so that young an Indian student does not get lost in the chaos of a new city. Finally, we would like to thank the referee for the detailed and thorough comments which have helped us in improving the manuscript.

9 DATA AVAILABILITY

The data underlying in this article are available in this article.

REFERENCES

- Abazajian K. N., et al., 2016, arXiv e-prints, p. [arXiv:1610.02743](https://arxiv.org/abs/1610.02743)
 Abazajian K., et al., 2019, arXiv e-prints, p. [arXiv:1907.04473](https://arxiv.org/abs/1907.04473)
 Ade P., et al., 2019, *JCAP*, **2019**, 056
 Aghanim N., Desert F. X., Puget J. L., Gispert R., 1996, *A&A*, **311**, 1
 Aghanim N., Majumdar S., Silk J., 2008, *Reports on Progress in Physics*, **71**, 066902
 Aghanim N., et al., 2018, preprint, ([arXiv:1807.06209](https://arxiv.org/abs/1807.06209))
 Baldwin J. E., 1982, in Heeschen D. S., Wade C. M., eds, IAU Symposium Vol. 97, Extragalactic Radio Sources. pp 21–24
 Begelman M. C., Cioffi D. F., 1989, *ApJL*, **345**, L21
 Birkinshaw M., 1999, *Physics Reports*, **310**, 97
 CMB Bharat Consortium, Exploring Cosmic History and Origin 2018, www.cmb-bharat.in, accessed March 5, 2021
 Challinor A., Lasenby A., 1998, *ApJ*, **499**, 1
 Chluba J., Sunyaev R. A., 2012, *MNRAS*, **419**, 1294
 Chluba J., Khatri R., Sunyaev R. A., 2012, *MNRAS*, **425**, 1129
 Colafrancesco S., 2008, *MNRAS*, **385**, 2041
 Colafrancesco S., Marchegiani P., 2011, *A&A*, **535**, A108
 Colafrancesco S., Marchegiani P., de Bernardis P., Masi S., 2013, *A&A*, **550**, A92
 Croston J. H., Hardcastle M. J., Harris D. E., Belsole E., Birkinshaw M., Worrall D. M., 2005, *ApJ*, **626**, 733
 Dolgov A. D., Hansen S. H., Pastor S., Semikoz D. V., 2001, *ApJ*, **554**, 74

- EnBlin T. A., Kaiser C. R., 2000, *A&A*, **360**, 417
 Erler J., Basu K., Chluba J., Bertoldi F., 2018, *MNRAS*, **476**, 3360
 Erlund M. C., Fabian A. C., Blundell K. M., 2008, *MNRAS*, **386**, 1774
 Fabian A. C., Chapman S., Casey C. M., Bauer F., Blundell K. M., 2009, *MNRAS*, **395**, L67
 Felten J. E., Rees M. J., 1969, *Nature*, **221**, 924
 Fixsen D. J., Cheng E. S., Gales J. M., Mather J. C., Shafer R. A., Wright E. L., 1996, *ApJ*, **473**, 576
 Fukazawa Y., Makishima K., Ohashi T., 2004, *PASJ*, **56**, 965
 Hanany S., et al., 2019, arXiv e-prints, p. [arXiv:1902.10541](https://arxiv.org/abs/1902.10541)
 Hardcastle M. J., Croston J. H., 2020, arXiv e-prints, p. [arXiv:2003.06137](https://arxiv.org/abs/2003.06137)
 Illarionov A. F., Siuniae R. A., 1975, *Soviet Astronomy*, **18**, 413
 Isobe N., Tashiro M. S., Gandhi P., Hayato A., Nagai H., Hada K., Seta H., Matsuta K., 2009, *ApJ*, **706**, 454
 Itoh N., Kohyama Y., Nozawa S., 1998, *ApJ*, **502**, 7
 Jetha N. N., Ponman T. J., Hardcastle M. J., Croston J. H., 2007, *MNRAS*, **376**, 193
 Johnson O., Almaini O., Best P. N., Dunlop J., 2007, *MNRAS*, **376**, 151
 Kaiser C. R., Alexander P., 1997, *MNRAS*, **286**, 215
 Kaiser C. R., Dennett-Thorpe J., Alexander P., 1997, *MNRAS*, **292**, 723
 Khatri R., Sunyaev R. A., Chluba J., 2012, *A&A*, **543**, A136
 Leahy J. P., Williams A. G., 1984, *MNRAS*, **210**, 929
 Majumdar S., 2001, PhD thesis (Indian Institute of Science, Bangalore)
 Majumdar S., Nath B. B., Chiba M., 2001, *Monthly Notices of the Royal Astronomical Society*, **324**, 537
 Malu S., Datta A., Colafrancesco S., Marchegiani P., Subrahmanyam R., Narasimha D., Wieringa M. H., 2017, *Scientific Reports*, **7**, 16918
 Mroczkowski T., et al., 2019, *Space Sci. Rev.*, **215**, 17
 Nath B. B., 1995, *MNRAS*, **274**, 208
 Nath B. B., 2010, *MNRAS*, **407**, 1998
 Reynolds C. S., Begelman M. C., 1997, *ApJL*, **487**, L135
 Sazonov S. Y., Sunyaev R. A., 1998, *ApJ*, **508**, 1
 Scheuer P. A. G., 1974, *MNRAS*, **166**, 513
 Sunyaev R. A., Zeldovich Y. B., 1970, *ApSS*, **7**, 20
 Sunyaev R. A., Zeldovich I. B., 1980, *MNRAS*, **190**, 413
 Wang Y., Kaiser C. R., 2008, *MNRAS*, **388**, 677
 Yamada M., Sugiyama N., Silk J., 1999, *ApJ*, **522**, 66
 Zeldovich Y. B., Sunyaev R. A., 1969, *ApSS*, **4**, 301

This paper has been typeset from a $\text{\TeX}/\text{\LaTeX}$ file prepared by the author.